Electronic Supplementary Material (ESI) for Chemical Science.

Supplementary Information

Isolation of the elusive bisbenzimidazole $Bbim^{3-\bullet}$ radical anion and its employment in a metal complex

Florian Benner and Selvan Demir*

Department of Chemistry, Michigan State University, 578 S Shaw Lane, East Lansing, Michigan 48824, USA

*Correspondence to: sdemir@chemistry.msu.edu (S.D.)

Chem. Sci.

Table of Contents

1.1 Single crystal X-ray crystallography

Table S1: Crystallographic data and structural refinement of $(Cp^*_2Y)_2(\mu\text{-Bbim})$ • toluene, **1** and $[K(crypt\text{-}222)][(Cp^*_2Y)_2(\mu\text{-Bbim}^{\bullet})]$ • 3 THF, **2**.

Compound	**1**	**2**
CCDC no.	2123273	2123274
Empirical formula	$C_{61}H_{75}N_4Y_2$	$C_{84}H_{126.5}KN_6O_9Y_2$
Formula weight	1042.07	1582.84
Temperature/K	173.15	100.00(10)
Crystal system	triclinic	triclinic
Space group	*P*-1	*P*-1
a [Å]	10.5717(10)	13.0300(2)
b [Å]	11.0365(10)	18.0681(4)
c [Å]	12.4271(12)	18.3710(3)
α [°]	67.8112(11)	86.907(2)
β [°]	87.4492(12)	78.0500(10)
γ [°]	79.2874(12)	76.349(2)
Volume [Å^3]	1318.6(2)	4111.72(13)
Z	1	2
ρ_{calc} [g/cm^3]	1.312	1.278
μ [mm^{-1}]	2.232	1.513
F(000)	547.0	1683.0
Crystal size [mm^3]	0.245 × 0.222 × 0.122	0.145 × 0.119 × 0.084
Radiation	MoK_α (λ = 0.71073)	MoK_α (λ = 0.71073)
2Θ range for data collection [°]	3.54 to 50.734	4.348 to 61.854
Index ranges	-12 ≤ *h* ≤ 12, -13 ≤ *k* ≤ 13, -14 ≤ *l* ≤ 14	-17 ≤ *h* ≤ 18, -25 ≤ *k* ≤ 22, -25 ≤ *l* ≤ 25
Reflections collected	21396	82579
Independent reflections	4822 [R_{int} = 0.0617, R_σ = 0.0535]	21330 [R_{int} = 0.0430, R_σ = 0.0443]
Data/restraints/parameters	4822/0/336	21330/0/966
Goodness-of-fit on F^2	1.053	1.028
Final *R* indexes [$I >= 2\sigma(I)$]	R_1 = 0.0457, wR_2 = 0.1085	R_1 = 0.0458, wR_2 = 0.1038
Final *R* indexes [all data]	R_1 = 0.0616, wR_2 = 0.1170	R_1 = 0.0641, wR_2 = 0.1102
Largest diff. peak/hole [e Å^{-3}]	0.90/−0.42	1.60/−0.52

1.2 NMR Spectroscopy

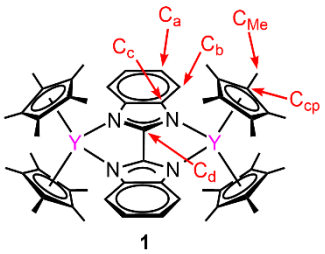

1

Figure S1. NMR numbering scheme for $(Cp^*_2Y)_2$(μ-Bbim), **1**.

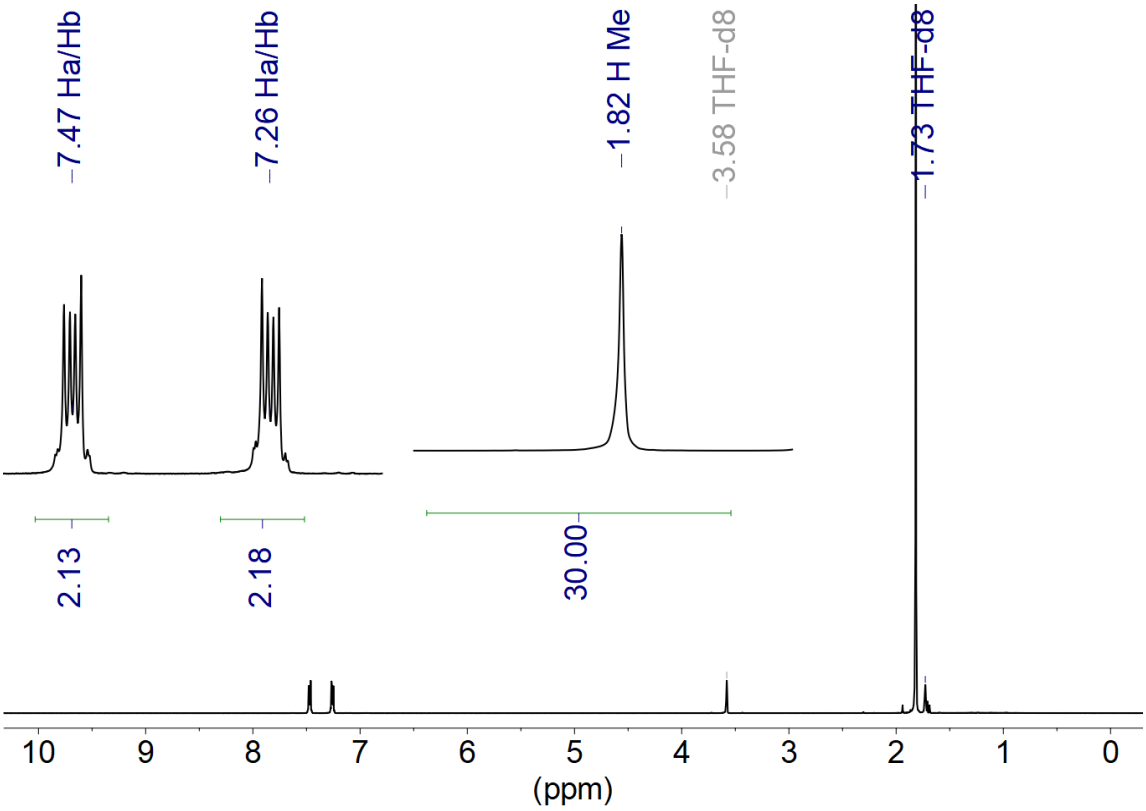

Figure S2. ^{1}H-NMR spectrum of $(Cp^*_2Y)_2$(μ-Bbim), **1** (500 MHz, 25 °C, THF-d_8).

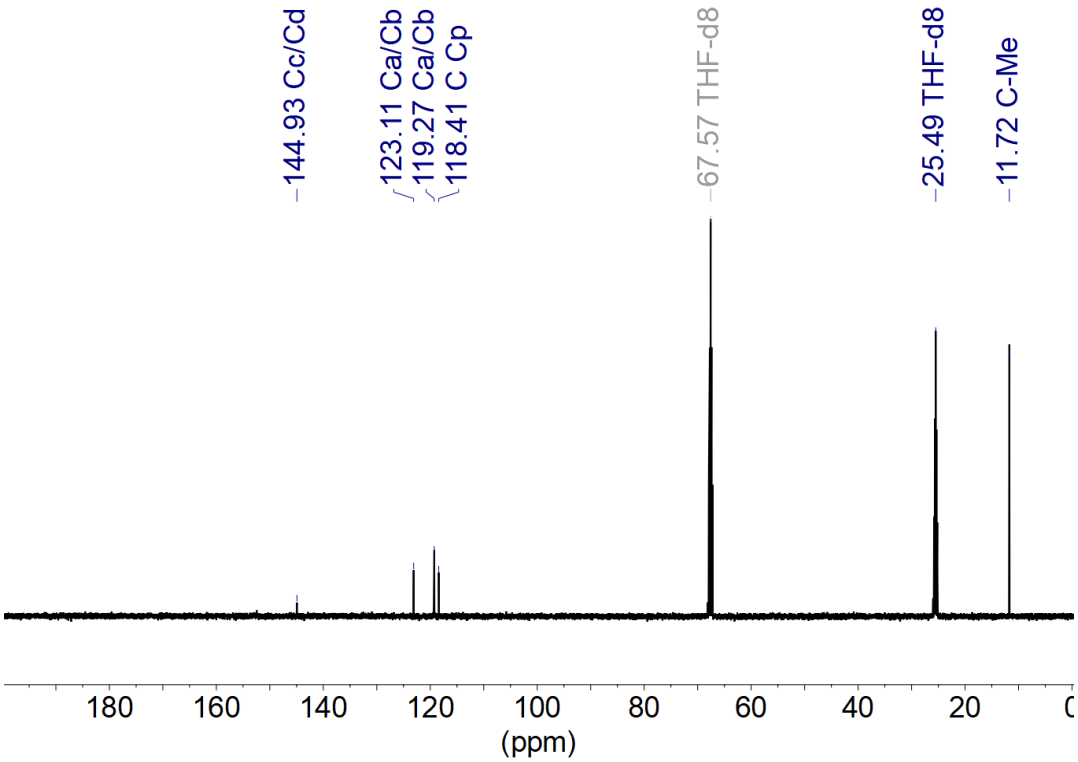

Figure S3. ^{13}C-NMR spectrum of (Cp*$_2$Y)$_2$(μ-Bbim), **1** (125 MHz, 25 °C, THF-d_8).

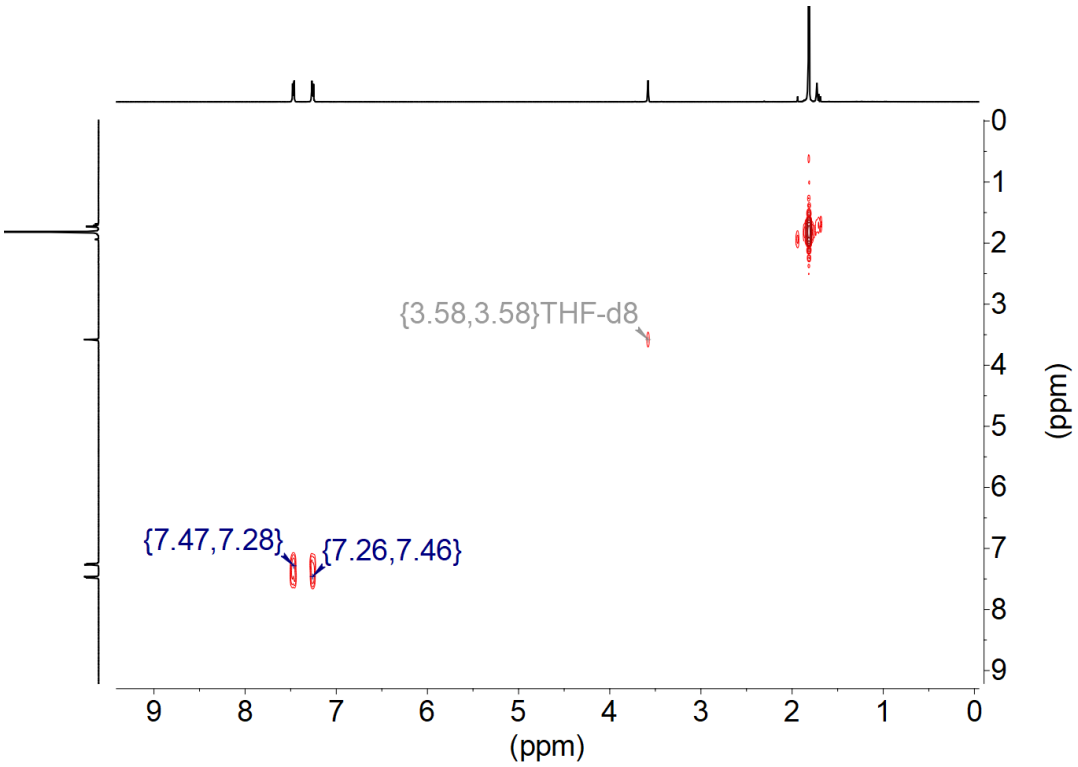

Figure S4. ^{1}H/^{1}H-COSY-NMR spectrum of (Cp*$_2$Y)$_2$(μ-Bbim), **1** (500 MHz, 25 °C, THF-d_8).

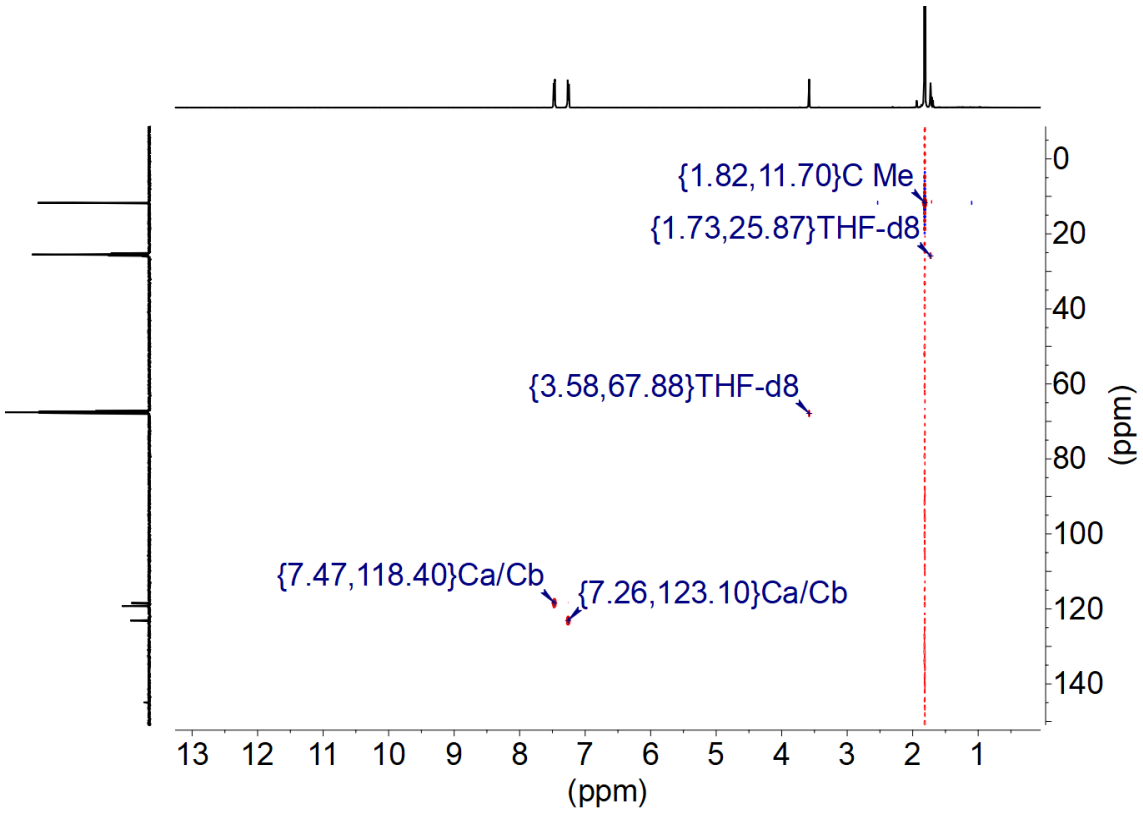

Figure S5. $^{1}H/^{13}C$-HSQC-NMR spectrum of $(Cp^{*}_{2}Y)_{2}$(μ-Bbim), **1** (500 MHz, 25 °C, THF-d_8).

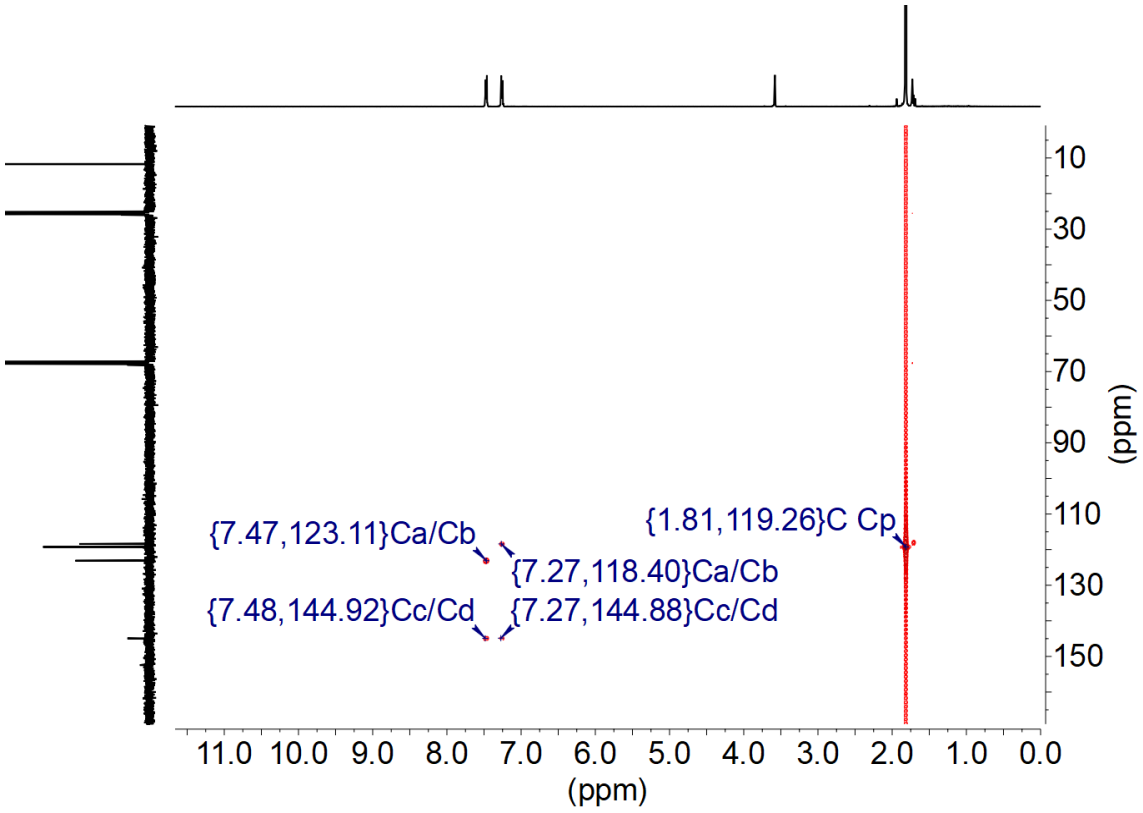

Figure S6. $^{1}H/^{13}C$-HMBC-NMR spectrum of $(Cp^{*}_{2}Y)_{2}$(μ-Bbim), **1** (500 MHz, 25 °C, THF-d_8).

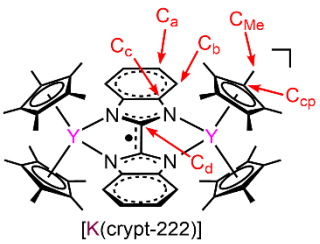

Figure S7. NMR numbering scheme for [K(crypt-222)][(Cp*$_2$Y)$_2$(μ-Bbim$^•$)], **2**.

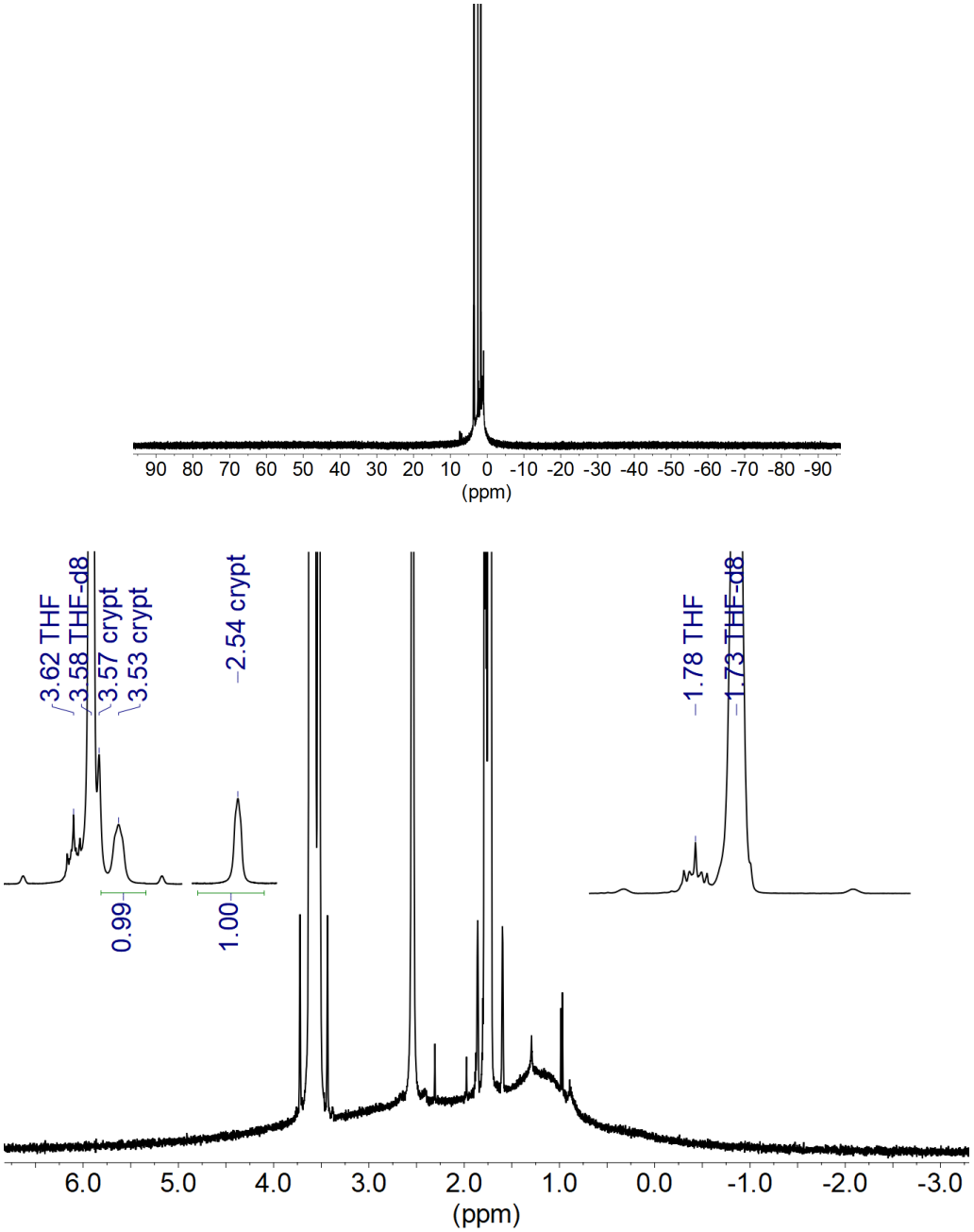

Figure S8. Top: Full ^{1}H-NMR spectrum of [K(crypt-222)][(Cp*$_2$Y)$_2$(μ-Bbim$^•$)], **2** (500 MHz, 25 °C, THF-d_8). Bottom: Magnification of the 6.5 and –3.0 ppm region.

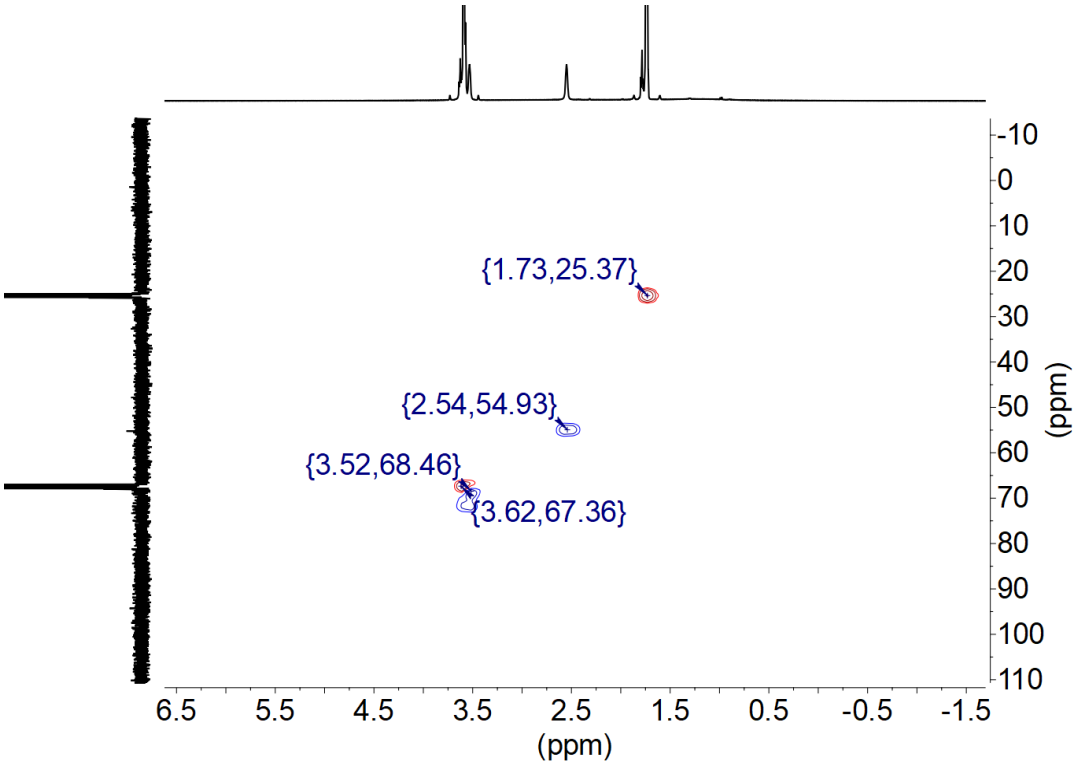

Figure S9. $^{1}H/^{13}C$-HSQC-NMR spectrum of [K(crypt-222)][$(Cp^*_2Y)_2$(μ-Bbim$^{\bullet}$)], **2** (500 MHz, 25 °C, THF-d_8).

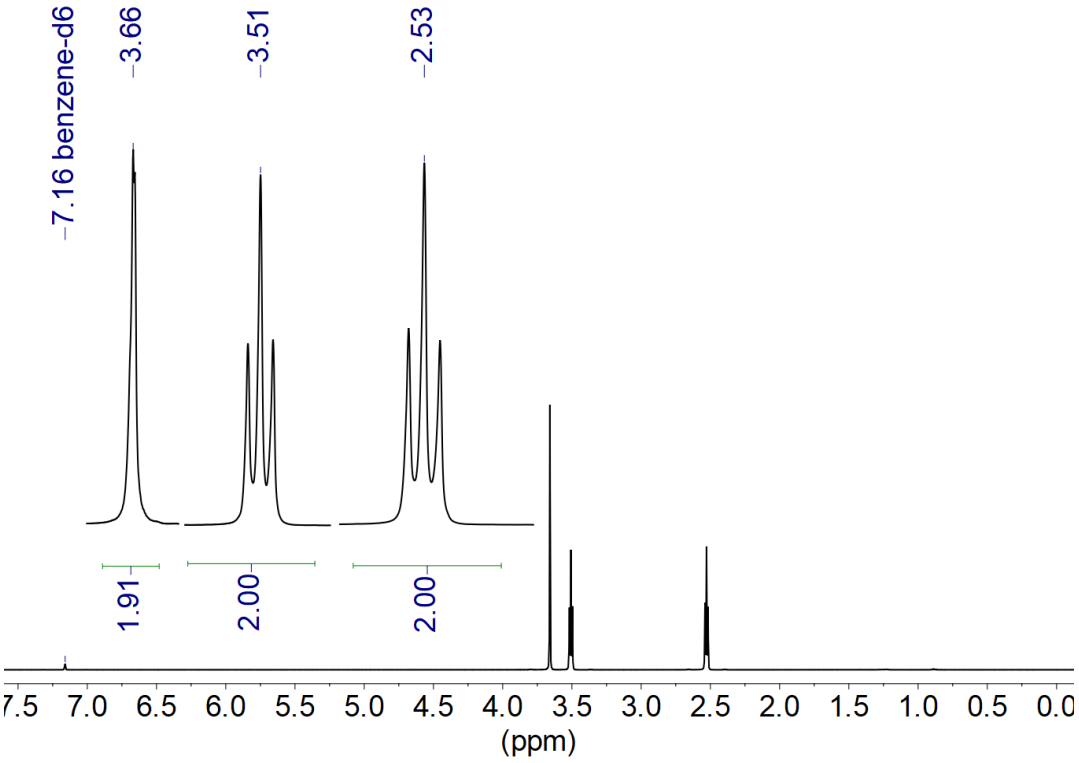

Figure S10. ^{1}H-NMR spectrum of 2.2.2-cryptand for reference (500 MHz, 25 °C, benzene-d_6).

1.3 EPR Spectroscopy

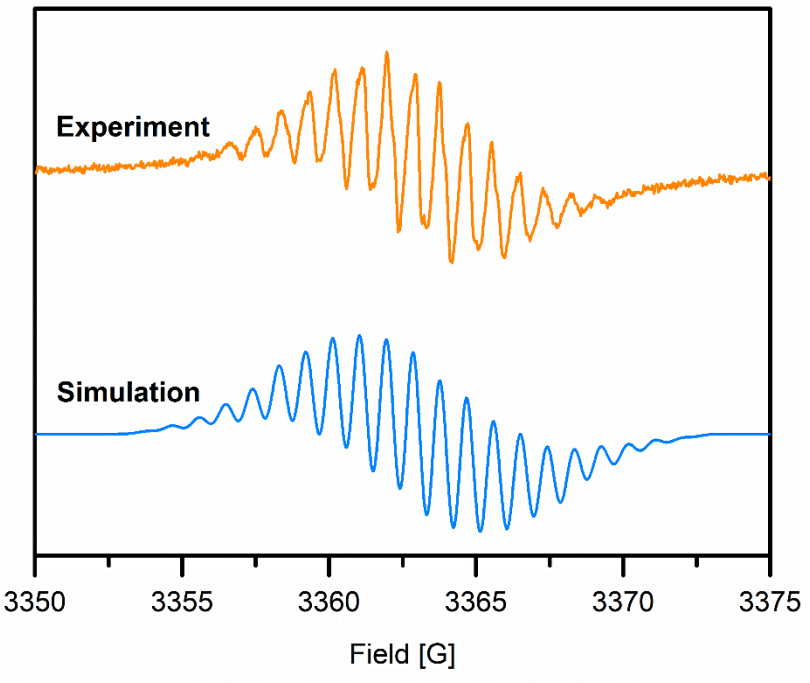

Figure S11. Low-temperature EPR spectrum of [K(crypt-222)][(Cp*$_2$Y)$_2$(μ-Bbim$^•$)], **2**, measured at 190 K. In orange: The experimental spectrum recorded in THF at 9.439 GHz. In blue: Simulated spectrum. Simulation parameters: 4 ^{14}N, 4 ^{1}H$_1$, 4 ^{1}H$_2$ and 2 ^{89}Y nuclei, A(^{14}N) = 5.1 MHz, A_1(^{1}H) = 2.30 MHz, A_2(^{1}H) = 0.54 MHz, A(^{89}Y) = 0.42 MHz), g = 2.00536 (298 K), linewidth: 0.07 mT.

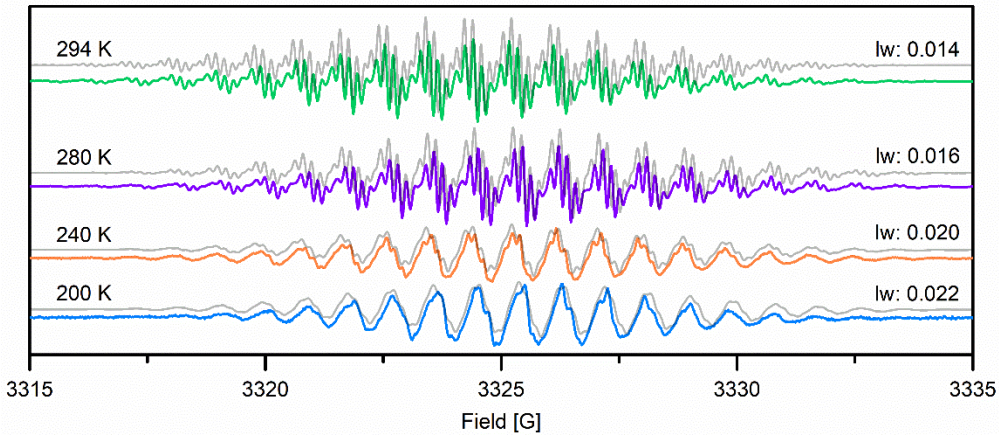

Figure S12. Variable-temperature EPR spectra of [K(crypt-222)][(Cp*$_2$Y)$_2$(μ-Bbim$^•$)], **2**, (in color, Fig. 4 top), superimposed with the fits for each temperature (faded traces in gray, Fig. 4 bottom). The experimental spectra were recorded in THF at 9.335 GHz (200-280K) and 9.331 GHz (294 K). Simulation parameters: 4 ^{14}N, 4 ^{1}H$_1$, 4 ^{1}H$_2$ and 2 ^{89}Y nuclei, A(^{14}N) = 5.1 MHz, A_1(^{1}H) = 2.30 MHz, A_2(^{1}H) = 0.54 MHz, A(^{89}Y) = 0.42 MHz), g = 2.00554 (294 K), 2.00557 (280-200 K), linewidths (lw) are given in mT.

1.4 Integration of Experimental EPR Spectra

The experimental EPR spectra of Figure S12 can be integrated to give the integrated derivative and double-integrated VT EPR spectra in the temperature range of 200 K to 280 K, Figure S13. The absorption spectra uncover the changes in line shapes and the accompanied loss in resolution. The double-integrated EPR spectra allow for the quantification of the intensity. These spectra reveal a correlation of resolution loss and reduced signal intensity to a decline in temperature. A loss of intensity could indicate a temperature-dependent formation of radical dimers in solution, affording an EPR silent species which diminishes the overall signal intensity. Such reversible dimerization interactions have been investigated for planar aromatic radicals such as phenalenyl-[1] and olympicenyl[2] radicals, where VT EPR spectroscopy enabled the determination of dimerization constants. However, this formation of EPR silent dimers would not affect the hyperfine coupling pattern of the parent complex as the EPR active monomeric species would remain unchanged. Since the hyperfine coupling pattern of **2** uniformly changes with varying temperature, it is more likely that the correlation time of the rotational diffusion becomes long enough, so that not all anisotropic contributions are averaged out (slow motion regime). The rotational correlation time τ_C is dependent on the rotational diffusion rate constant R by $\tau_C = 1/6_R$ and, in conjunction with the rigid-limit spectral width $\Delta\omega$, determines the shape of a CW EPR spectrum. When $\tau_C\Delta\omega \gg 1$, the rotational diffusion has negligible influence on the spectrum and it resembles the one in the rigid limit ($\tau_C \rightarrow \infty$, solid state like), whereas when $\tau_C\Delta\omega \leq 1$, the motion is fast enough to average out most anisotropic contributions ($\tau_C \rightarrow 0$, solution state like). The intermediate regime $1 < \tau_C\Delta\omega < 100$ is considered as the slow motion regime, where the spectrum is sensitive to rotational motion.[3–5] In this slow motion region, the EPR signal intensity is a complex interplay between correlation time, hyperfine coupling tensor anisotropy and the utilized magnetic field modulation amplitude. Taken together, most of the decrease in intensity observed in this experiment is attributed to a general loss in resolution due to incomplete averaging of hyperfine anisotropy. Based on the results of this measurement, the effects of a dimerization in solution cannot be entirely excluded, however, it should be noted that a dimerization is generally substantially hampered by the two coordinating Cp* ligands per metal center. Since no additional signals emerge from the EPR spectra upon lowering the temperature, as for example observed for the phenalenyl[1] radical, the formation of a new EPR active dimer through π-stacking with a neutral $[(Cp^*_2Y)_2(\mu\text{-Bbim})]$ can be excluded.

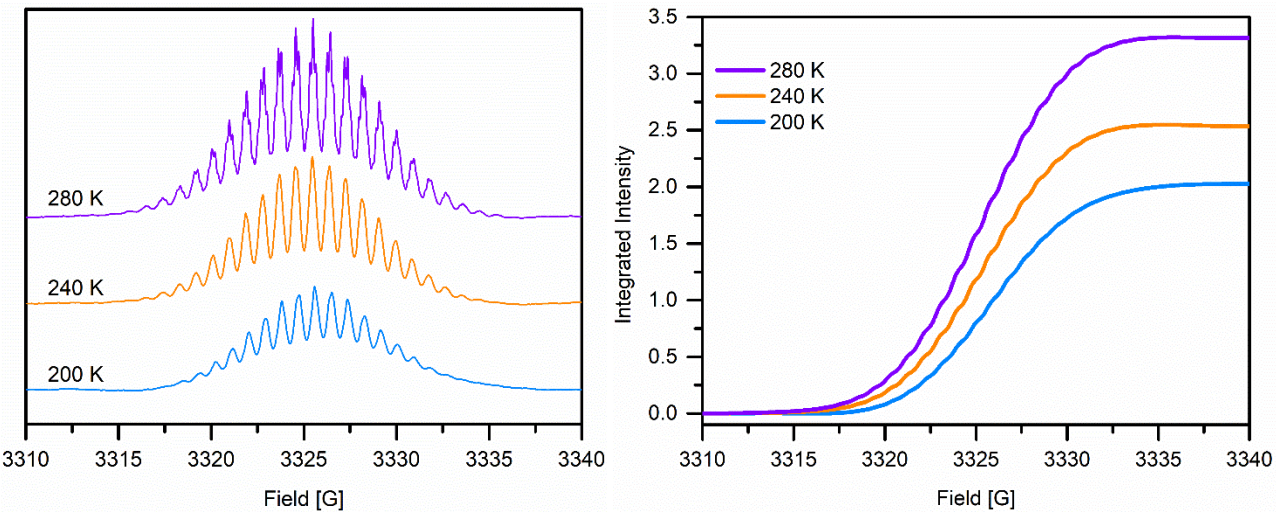

Figure S13. Integrated derivative (left) and double-integrated (right) VT EPR spectra at 280 K, 240 K, and 200 K, which were obtained from integrating the experimental spectra shown in Figure S12 (taken in THF at 1 mmol/L concentration).

Table S2. Values for the integrated intensity of the VT EPR experiments between 200 K and 280 K and the linewidths used to simulate the EPR spectra for **2** as full width at half maximum (FWHM) in mT. The intensity loss of approximately 40% by lowering the temperature from 280 K and 200 K could indicate a radical dimer formation in solution.

Temperature (K)	Integrated Intensity	% Intensity loss vs. 280 K	Line Width (mT)
280	3.319	0	0.016
240	2.548	23.2	0.020
200	2.027	38.9	0.022

1.5 Magnetic Measurements

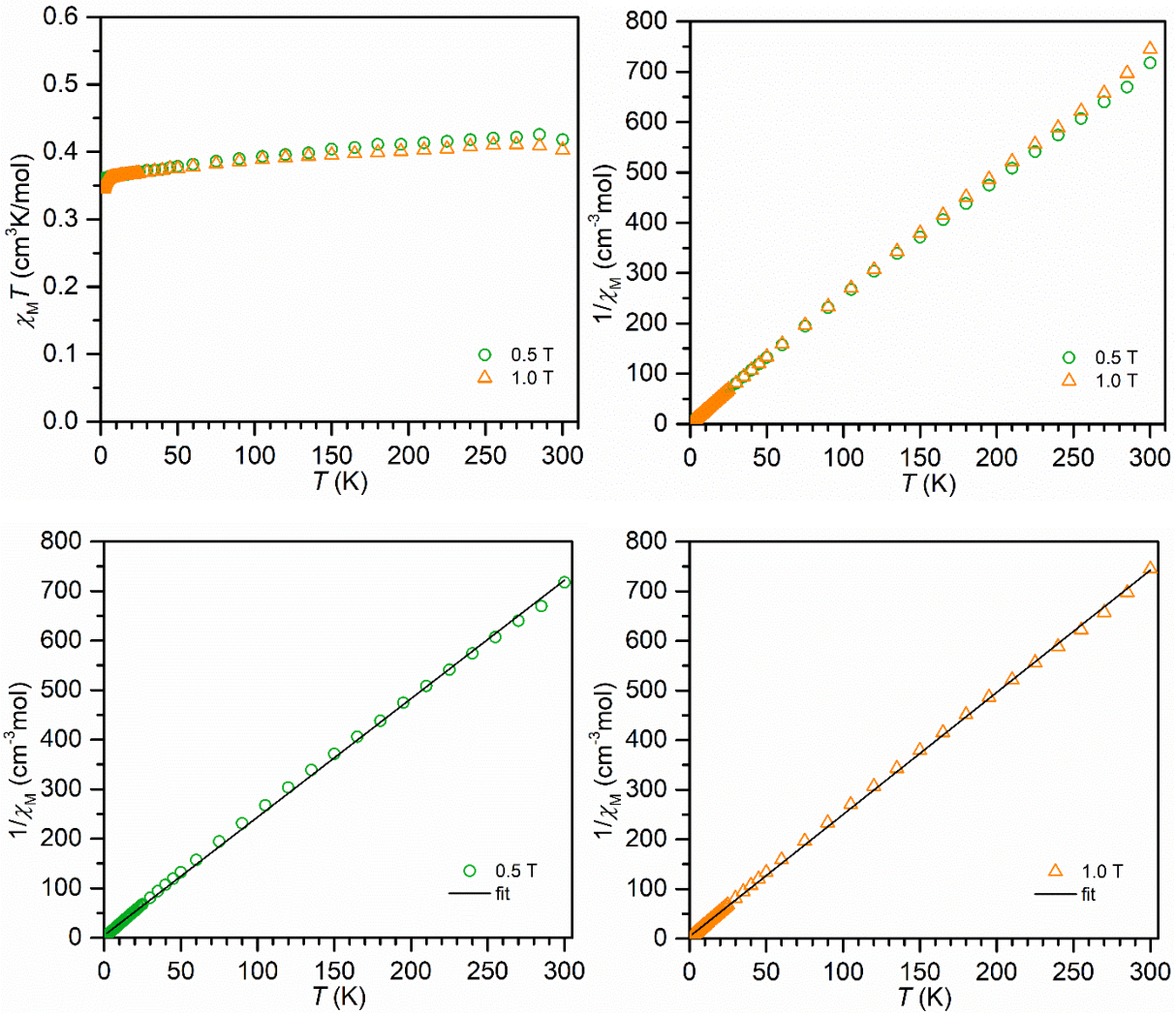

Figure S14. Top: $\chi_M T$ vs. T plots (left) and Curie-Weiss-plots ($1/\chi_M$ vs. T, right) for [K(crypt-222)][(Cp*$_2$Y)$_2$(μ-Bbim$^•$)], **2**, obtained between 2 and 300 K under applied dc fields of 0.5 T (green circles) and 1.0 T (yellow triangles). Bottom: Fits of the $1/\chi_M$ vs. T plots to a Curie-Weiss Law at 0.5 T (left) and 1.0 T (right). The room temperature χ_MT values of **2** were found to be slightly higher than the expected value for one unpaired electron (0.419 cm^{3}K/mol (0.5 T) and 0.403 cm^{3}K/mol (0.1 T), calculated: 0.375 cm^{3}K/mol). The Curie-Weiss plot reveals a gradual decrease in $1/\chi_M$ upon decreasing temperatures, as expected for a paramagnetic compound. Deviations from linearity were primarily observed for the lower applied DC field (0.5 T) and are in line with the deviations observed for the room temperature $\chi_M T$ values. Fitting the $1/\chi_M$ values to a Curie-Weiss law revealed small negative Weiss constants, indicative of the presence of weak intermolecular antiferromagnetic coupling. These values showed a field dependence, where increasingly strong fields reduce the Θ values. This hints at an increasing suppression of the intermolecular coupling which has been observed before for single-molecule magnets containing paramagnetic metal ions such as lanthanides, where the suppression of intermolecular magnetic coupling was found to alter relaxation dynamics upon the application of an external magnetic field.[6]

Table S3. Curie (C) and Weiss (Θ) constants obtained from fitting the $1/\chi_M$ vs. T data to a Curie-Weiss Law ($1/\chi_M = (T-\theta)/C$) with squared errors (R^2) as indication for the goodness of the fits.

Field (T)	C (cm^3K/mol)	Θ (K)	R^2
0.5	0.418	−1.897	0.99932
1.0	0.406	−1.492	0.99962

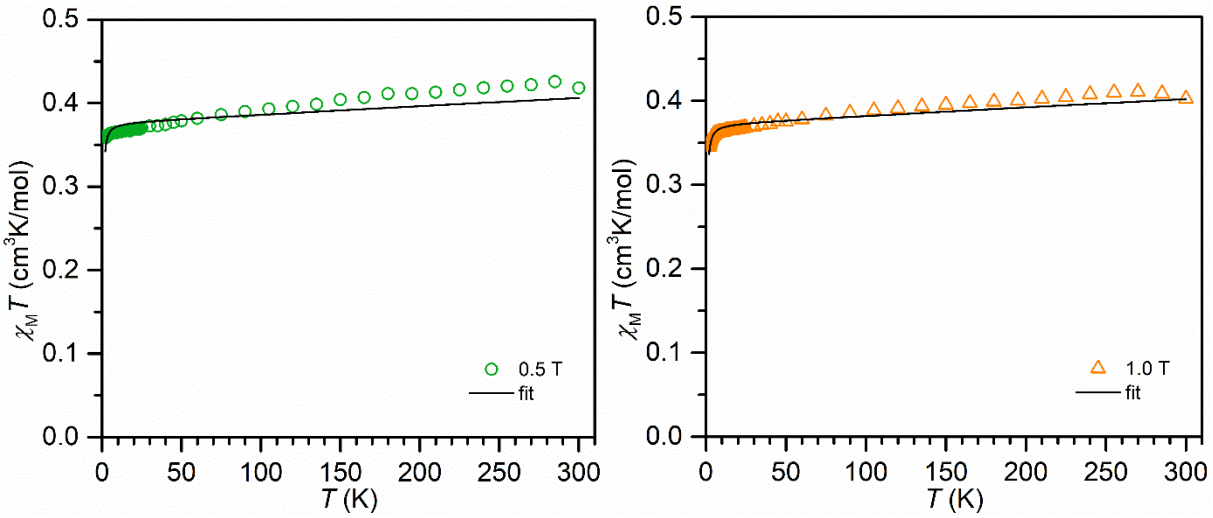

Figure S15. Fits to the $\chi_M T$ vs. T plots considering the intermolecular coupling term zJ' and the g-value (left (0.5 T)) and right (1 T).

Table S4. g-values and mean-field intermolecular interaction between spin systems (zJ'), obtained from fitting the $\chi_M T$ vs. T plots using the software Phi[7] over the entire probed temperature range (2-300 K). A small constant temperature-independent paramagnetism term (TIP) was included to attain the best fit to the $\chi_M T$ data. Both the negative Θ values and small negative zJ' values indicate a small intermolecular coupling between the unpaired electrons in the solid state.

Field (T)	zJ' (cm^{-1})	g	Residual	TIP(10^{-4} cm^{-1})
0.5	–0.088(12)	2.0035(28)	0.005726	1
1.0	–0.098(8)	1.9927(17)	0.002101	1

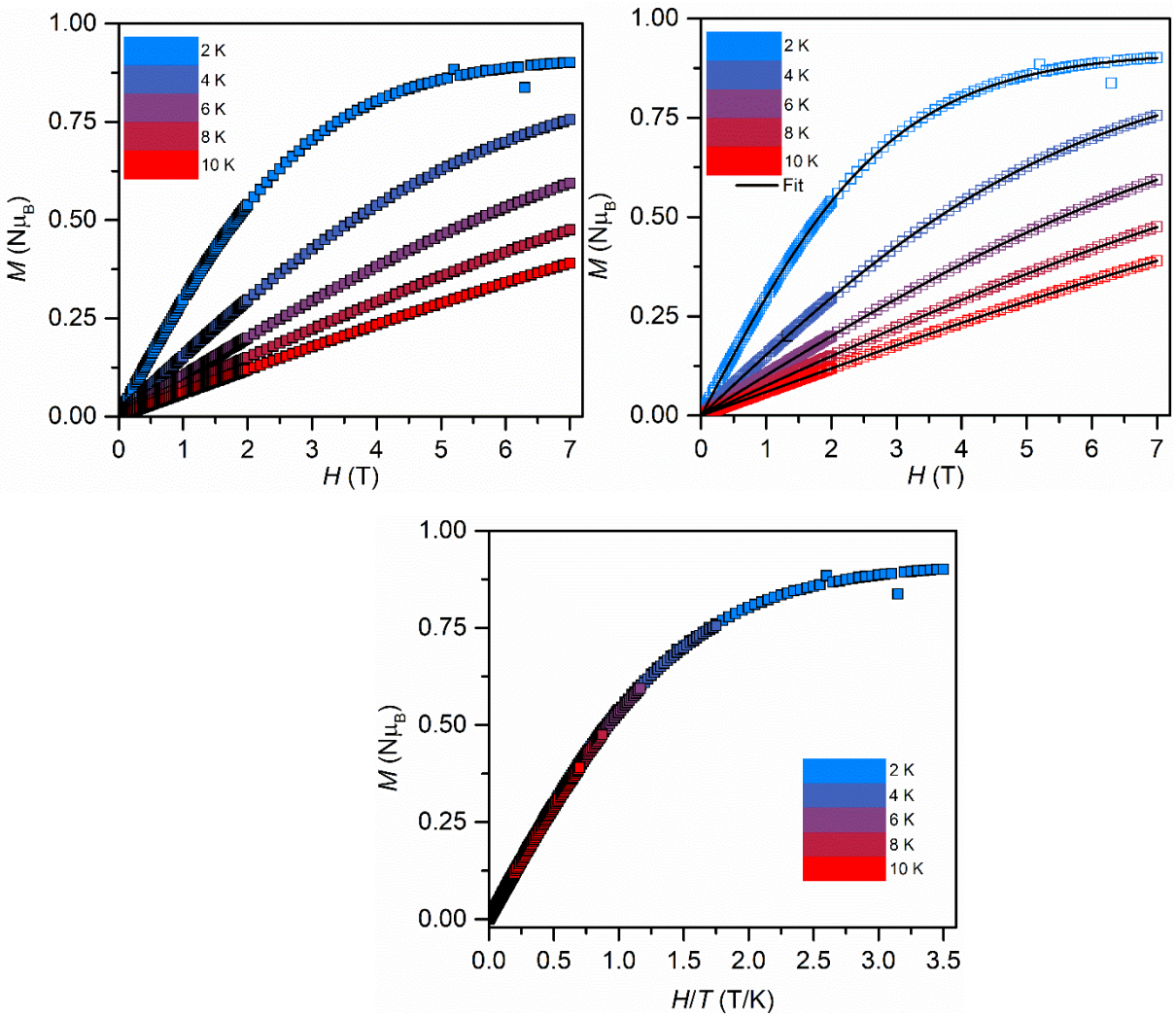

Figure S16. Field-dependent magnetization (*M* vs. *H*) data (top, left) with the corresponding fit to a Brillouin function (top, right) and reduced magnetization (*H*/*T*) data (bottom) for [K(crypt-222)][(Cp*$_2$Y)$_2$(μ-Bbim$^•$)], **2**, collected from 2 K (blue squares) to 10 K (red squares) in 2 K increments and under fields of 0 to 7 T. The reduced magnetization plot reveals that all measured magnetization curves superimpose to one single curve as expected for an organic radical with negligible magnetic anisotropy.

Table S5. *g*-Values and number of moments (*N*) obtained from fitting the *M* vs. *H* data to a Brillouin function with squared errors (R^2) as a measure for the goodness of the fits. The total angular momentum quantum number *J* was set to ½ for one unpaired electron. The field dependence of the magnetization is well-described by the Brillouin function for all probed temperatures. From these fits, *N* values were found to range between 0.89 and 0.91, indicating that approximately 90% of the non-interacting radical spins contribute to the Curie-Weiss susceptibility within the investigated temperature range.

Temperature (K)	*g*	*N*	R^2
2	2.0069(55)	0.9135(36)	0.99974
4	2.0078(10)	0.9090(8)	0.99999
6	2.0108(15)	0.8981(12)	0.99999
8	2.0023(28)	0.8964(24)	0.99999
10	2.0037(33)	0.8858(28)	0.99999

1.6 IR Spectroscopy

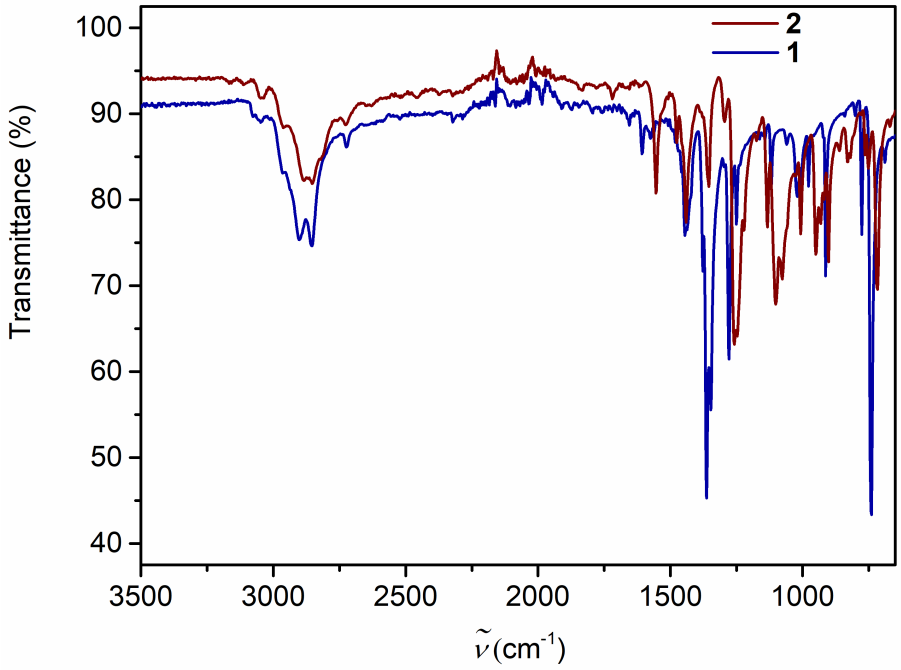

Figure S17. FTIR spectra of $(Cp^*_2Y)_2$(μ-Bbim), **1** (dark blue) and [K(crypt-222)][$(Cp^*_2Y)_2$(μ-Bbim$^{\bullet}$)], **2**, (dark red).

1.7 Cyclic Voltammetry

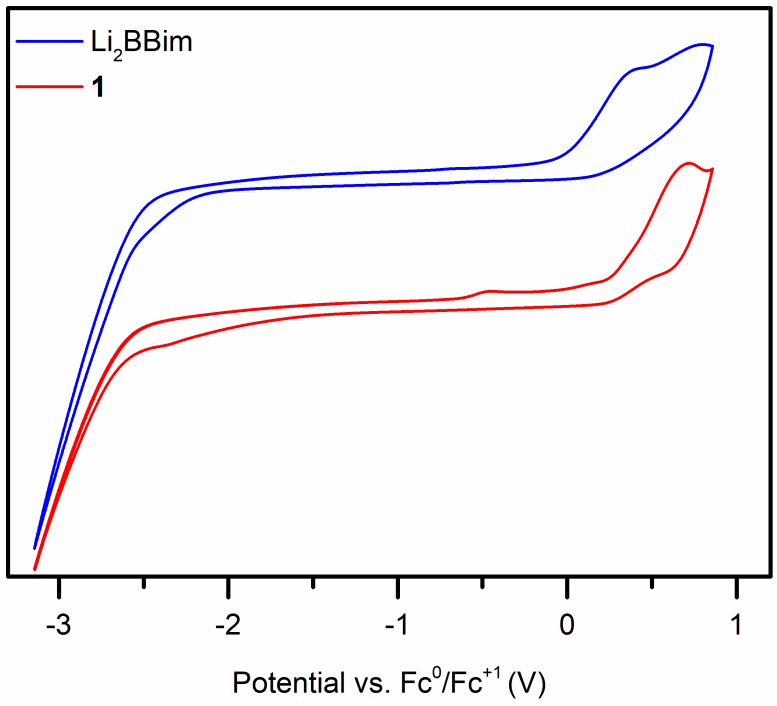

Figure S18. Cyclic voltammogram of the free ligand $(Li(TMEDA))_2$Bbim (blue) and $(Cp^*_2Y)_2(\mu$-Bbim), **1**, (red) in dichloromethane**.**

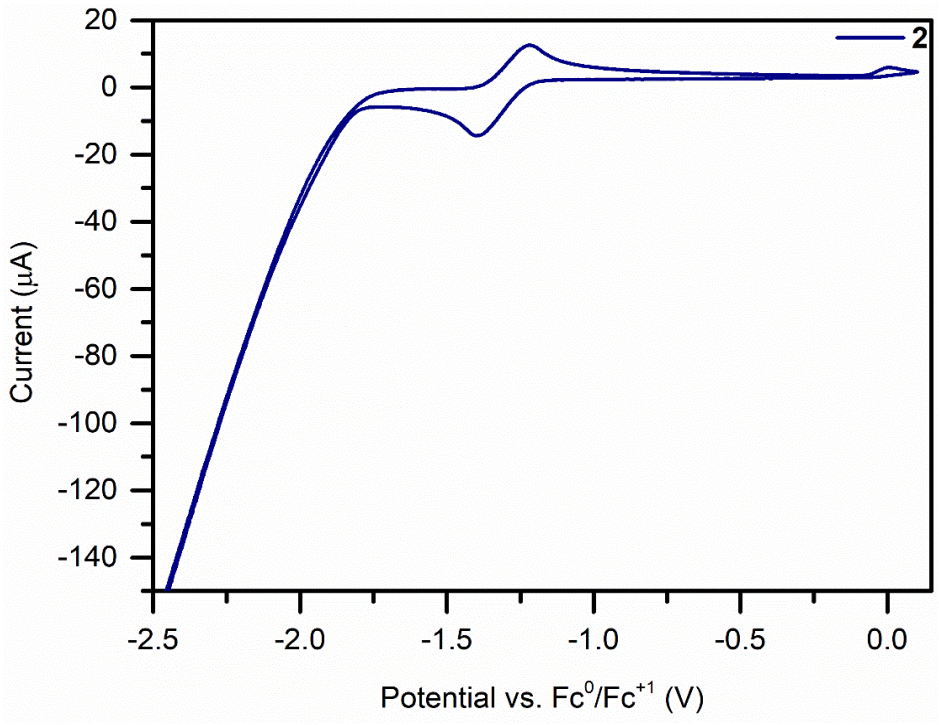

Figure S19. Full cyclic voltammogram of $[K(crypt\text{-}222)][(Cp^*_2Y)_2(\mu\text{-}Bbim^{\bullet})]$, **2**, measured in THF. Magnification is depicted in Figure 6 in the main text.

1.8 DFT calculations

As described in the main text, structural optimizations were carried on a simplified model of **2** where all Cp* methyl groups were substituted by H atoms (herein called **2'**). In comparison to the initial structure obtained from single crystal X-ray analysis, the DFT methods predict a slightly differing conformation of the bridging $Bbim^{3-\bullet}$, presumably due to the reduced steric interaction imposed upon truncation in **2'** (Fig S21). With respect to the truncations imposed on **2'** the structural comparison (Tables S6 and S7) is limited to the Bbim and Y interactions while the inner Cp C–C-distances and -angles were not further analysed. The deployed approximations for the model complex evoked a slight displacement of the Y atoms below the Bbim plane, affording a "boat" conformation in the optimized structures and deviating from the zig-zag conformation uncovered by the crystal structure. This is also reflected in shortened Y1–Y2 distances (0.195-0.212 Å). These effects may be rationalized by the increased steric hinderance caused by the Cp* rings in **2** compared to the Cp moieties in **2'**, which also allows for closer proximity of the Cp ligands to the metal centres. To further validate the electronic structure of the optimized structures single point calculations were additionally carried out on the unoptimized heavy atom coordinates of **2'** as obtained from the crystal structure of **2** after replacing the Cp methyl groups by protons. In comparison to the nitrogen lone pair (LP) contributions obtained for the optimized structures the NLMO analysis of the unoptimized structures shows very comparable orbital contributions to the Y–interacting nitrogen LPs (Tables S13 and S14), further suggesting a negligible influence of the Cp* methyl groups to the Y–Bbim bonding. Lastly, in comparison to the hyperfine coupling parameters utilized for the simulation of the EPR spectra, DFT seems slightly overestimated the spin density delocalized onto the yttrium atoms, which might also be a consequence of the shorter calculated Y–N distances (0.0152–0.0184 Å).

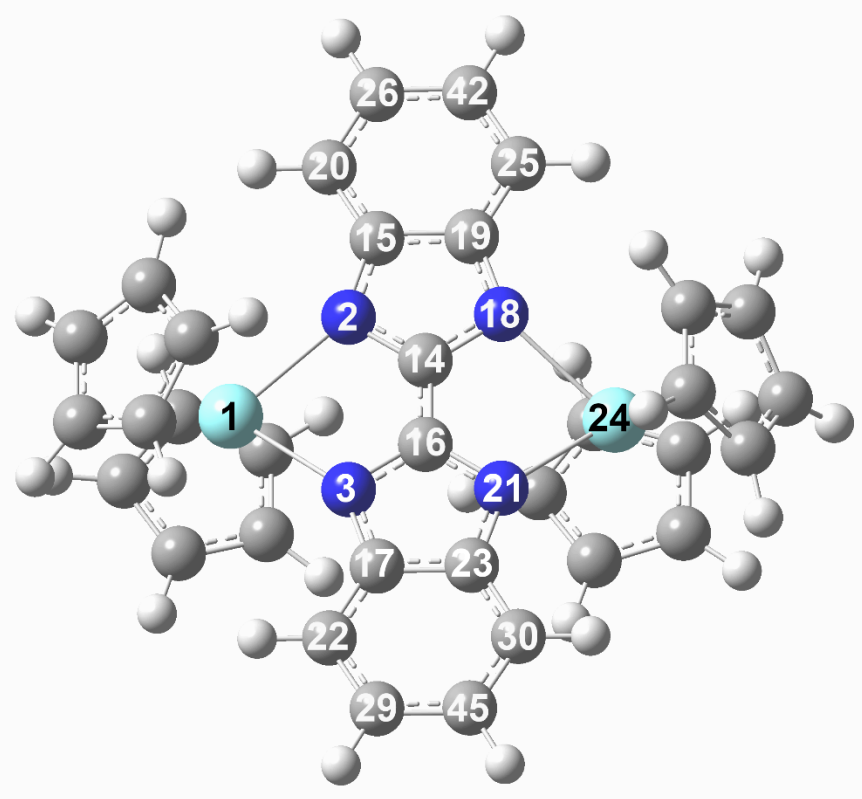

Figure S20. Numbering scheme as employed in structure optimizations and NLMO/spin density calculations.

Table S6. Structural parameters of the optimized geometries of **2'** in comparison to the experimental values for **2** as obtained from single-crystal X-ray crystallography. Positive signs represent longer calculated and negative values shorter calculated values compared to the experimental values. The highlighted cells in green represent the smallest deviation between experimental and calculated values while blue highlights the largest deviations.

Experimental Values		**Calculated**			
		uTPSS		**uB3LYP**	
Atoms	Distance (Å)	Distance (Å)	Difference	Distance (Å)	Difference
Y1-N2	2.3550(17)	2.3492	–0.0058	2.3436	–0.0114
Y1-N3	2.3639(18)	2.3492	–0.0147	2.3436	–0.0203
Y24-N10	2.3739(18)	2.3461	–0.0278	2.3454	–0.0285
Y24-N21	2.3586(17)	2.3461	–0.0125	2.3454	–0.0132
Avg. Y-N	2.3629(17)	2.3477	–0.0152	2.3455	–0.0184
N2-C14	1.3838(27)	1.3810	-0.0007	1.3804	-0.0034
C14-N18	1.3812(26)	1.3791	0.0035	1.3796	-0.0016
Avg. C14-N	1.3825(27)	1.3839	0.0014	1.3800	–0.0025
N3-C16	1.3838(26)	1.3831	–0.0007	1.3804	–0.0034
C16-N21	1.3813(27)	1.3847	0.0034	1.3796	–0.0017
Avg. C15-N	1.3826(27)	1.3839	0.0014	1.3800	–0.0025
N18-C19	1.3847(25)	1.3830	–0.0017	1.3781	–0.0066
C19-C25	1.3942(27)	1.4064	0.0122	1.4005	0.0063
C25-C42	1.4019(30)	1.4103	0.0084	1.4066	0.0047
C42-C26	1.3894(32)	1.4094	0.0200	1.4037	0.0143
C26-C20	1.3988(29)	1.4102	0.0114	1.4065	0.0077
C20-C15	1.4012(28)	1.4064	0.0052	1.4005	–0.0007
C15-C19	1.4276(30)	1.4396	0.0120	1.4358	0.0082
C15-N2	1.3768(24)	1.3831	0.0063	1.3780	0.0012
N3-C17	1.3824(26)	1.3831	0.0007	1.3780	–0.0044
C17-C22	1.3910(28)	1.4064	0.0154	1.4005	0.0095
C22-C29	1.4005(32)	1.4102	0.0097	1.4065	0.0060
C29-C45	1.3921(33)	1.4094	0.0173	1.4037	0.0116
C45-C30	1.4014(29)	1.4103	0.0089	1.4066	0.0052
C30-C23	1.3937(29)	1.4064	0.0127	1.4005	0.0068
C23-C17	1.4283(29)	1.4396	0.0113	1.4358	0.0075
C12-N21	1.3804(24)	1.3830	0.0026	1.3781	–0.0023
C14-C15	1.4024(26)	1.4178	0.0154	1.4105	0.0081
Y-Y distance	6.030(5)	5.8345	-0.1954	5.8128	-0.2171

Table S7. Bond- and dihedral angles of the optimized geometries of **2'** in comparison to the experimental values for **2** as obtained from single-crystal X-ray diffraction. Positive signs represent longer calculated and negative values shorter calculated values compared to the experimental values. The highlighted cells in green represent the smallest deviation between experimental and calculated values while blue highlights the largest deviations.

Experimental Values		**Calculated**			
		uTPSS		**uB3LYP**	
Atoms	Angle (°)	Value (°)	Difference	Value (°)	Difference
N3-Y1-N2	75.874(60)	77.1250	1.2510	76.8840	1.0100
N18-Y24-N21	75.682(59)	76.8720	1.1900	77.0418	1.3598
Avg. N-Y-N	75.778(60)	76.9985	1.2205	76.9629	1.1849
Y1-N2-N21-Y24	176.760(58)	153.2340	-23.5260	152.7840	–23.9760
Y1-N3-N18-Y24	175.17(59)	153.2340	-21.9360	158.7870	–16.3830
Avg. diagonal bending	175.965(59)	153.2340	–22.7310	155.7855	–20.1795
Y1-N2-N18-Y24	26.471(228)	4.8614	–21.6096	2.378	–24.0930
Y1-N3-N21-Y24	20.044(237)	4.8612	–15.1828	2.344	–17.7000
Avg. axial bending	23.2575(233)	4.8613	–18.3962	2.3610	–20.8965
Tilt angle BBim benzene planes	3.118(66)	Planar	3.118	Planar	3.118

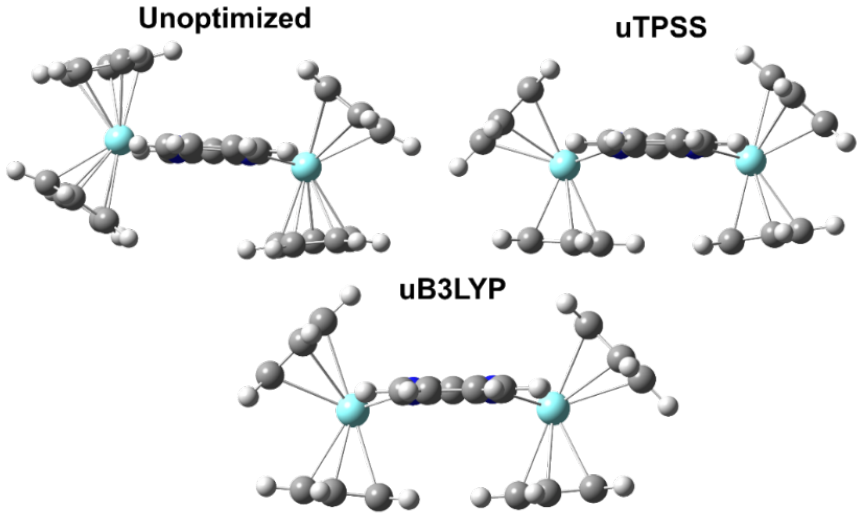

Figure S21. Graphical representation of the DFT optimized structures in comparison to the unoptimized structure (with Me for H substituted, all other coordinates are as obtained from single-crystal Xray analysis). The energy minimization led to a "boat"-like conformation for each functional, presumably due to reduced steric interaction of the Cp substituents.

Table S8. Results of the hybridization/polarization analysis of NLMOs, given as the % contributions of parent NBOs from uB3LYP calculations.

		NLMO contributions α manifold					**NLMO contributions β manifold**		
NLMO No.	Description	Y1	Y24	N	NLMO No.	Description	Y1	Y24	N
47	LP1 N2	7.29	0.06	90.38	47	LP1 N2	7.43	0.06	90.27
48	LP2 N2	2.19	0.32	78.38	48	LP1 N3	7.42	0.06	90.28
49	LP1 N3	7.22	0.06	90.41	51	LP1 N18	0.06	7.38	90.27
50	LP2 N3	2.23	0.33	78.41	53	LP1 N21	0.06	7.38	90.26
53	LP1 N18	0.07	7.24	90.43					
54	LP2 N18	0.25	2.35	77.59					
55	LP1 N21	0.07	7.23	90.43					
56	LP2 N21	0.24	2.32	77.58					

Table S9. Results of the second order perturbation analysis of **2'** from uB3LYP calculations. Only strongest interactions are shown (> 3 kcal/mol). Highlighted values show a significant discrepancy between α- and β-manifolds..

Donor NBO	Acceptor NBO	**E (kcal/mol) α manifold**	**E (kcal/mol) β manifold**
LP1 N2	LV1 Y1	15.44	15.96
LP2 N2	LV2 Y1	17.37	17.67
LP1 N2	LV5 Y1	18.88	19.11
LP1 N2	LV6 Y1	8.68	1.20
LP2 N2	LV4 Y1	4.25	-
LP1 N3	LV1 Y1	15.45	15.98
LP1 N3	LV2 Y1	17.36	17.64
LP1 N3	LV5 Y1	18.88	19.11
LP1 N3	LV6 Y1	8.68	1.20
LP1 N18	LV1 Y24	15.58	15.77
LP1 N18	LV2 Y24	16.90	17.37
LP1 N18	LV5 Y24	18.99	19.33
LP1 N18	LV6 Y24	12.30	1.23
LP2 N18	LV4 Y24	4.50	-
LP1 N21	LV1 Y24	15.58	15.77
LP1 N21	LV2 Y24	16.91	17.37
LP1 N21	LV5 Y24	18.99	19.33
LP1 N21	LV6 Y24	12.30	1.23
LP2 N21	LV4 Y24	4.50	-

Table S10. Results of the hybridization/polarization analysis of NLMOs, given as the % contributions of parent NBOs from uTPSS calculations.

		NLMO contributions α manifold					**NLMO contributions β manifold**		
NLMO No.	Description	Y1	Y24	N	NLMO No.	Description	Y1	Y24	N
47	LP1 N2	7.72	0.07	89.84	47	LP1 N2	7.80	0.06	89.78
48	LP2 N2	2.35	0.54	76.55	48	LP1 N3	7.79	0.06	89.79
49	LP1 N3	7.72	0.08	89.84	51	LP1 N18	0.07	7.70	89.79
50	LP2 N3	2.413	0.56	76.57	53	LP1 N21	0.07	7.70	89.79
53	LP1 N18	0.09	7.60	89.85					
54	LP2 N18	0.39	2.80	75.48					
55	LP1 N21	0.09	7.63	89.85					
56	LP2 N21	0.37	2.76	75.47					

Table S11. Results of the second order perturbation analysis of **2'** from uTPSS calculations. Only strongest interactions are shown (> 3 kcal/mol). Highlighted values show a significant discrepancy between α- and β-manifolds..

Donor NBO	Acceptor NBO	**E (kcal/mol) α manifold**	**E (kcal/mol) β manifold**
LP1 N2	LV1 Y1	13.96	13.81
LP2 N2	LV2 Y1	16.86	17.00
LP1 N2	LV5 Y1	19.49	19.43
LP1 N2	LV6 Y1	13.66	1.26
LP2 N2	LV4 Y1	4.19	-
LP1 N3	LV1 Y1	13.96	13.81
LP1 N3	LV2 Y1	16.86	17.00
LP1 N3	LV5 Y1	19.49	19.43
LP1 N3	LV6 Y1	13.66	1.26
LP2 N3	LV4 Y1	4.19	-
LP1 N18	LV1 Y24	13.84	13.04
LP1 N18	LV2 Y24	15.92	16.58
LP1 N18	LV5 Y24	15.13	19.40
LP1 N18	LV6 Y24	18.04	1.24
LP2 N18	LV3 Y24	4.30	-
LP1 N21	LV1 Y24	13.84	13.04
LP1 N21	LV2 Y24	15.92	16.58
LP1 N21	LV5 Y24	15.13	19.40
LP1 N21	LV6 Y24	18.04	1.24
LP2 N21	LV3 Y24	4.30	-

Table S12. Mulliken spin densities for **2'** with hydrogens summed into heavy atoms as obtained from NLMO calculations. The central atoms of the $Bbm^{3-\bullet}$ moiety were highlighted in green.

Atom	**uTPSS**	**uB3LYP**
Y1	0.054109	0.034287
N2	0.076381	0.090889
N3	0.076381	0.090890
C14	0.141857	0.157802
C15	–0.020075	–0.027685
C16	0.141857	0.157802
C17	–0.020075	–0.027684
N18	0.073368	0.089050
C19	–0.020381	–0.027935
C20	0.06617	0.067739
N21	0.073367	0.089049
C22	0.066117	0.067737
C23	–0.020381	–0.027936
Y24	0.079187	0.044648
C25	0.067251	0.068104
C26	0.018159	0.016672
C29	0.018159	0.016673
C30	0.067251	0.068105
C42	0.016123	0.015901
C45	0.016123	0.015899

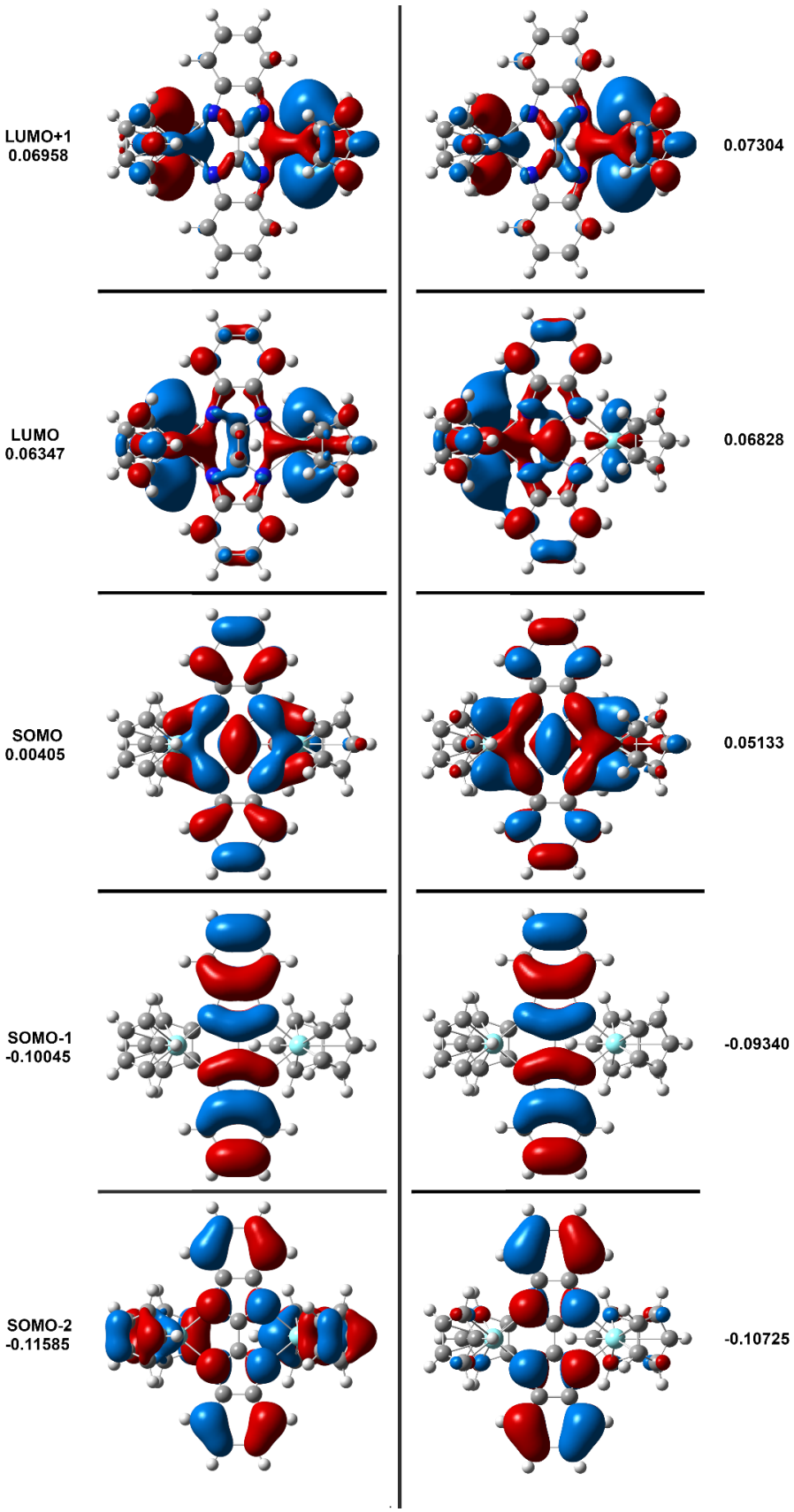

Figure S22. Graphical representation of the calculated B3LYP MOs of the α- (left) and β-manifold (right), sorted by their relative energies.

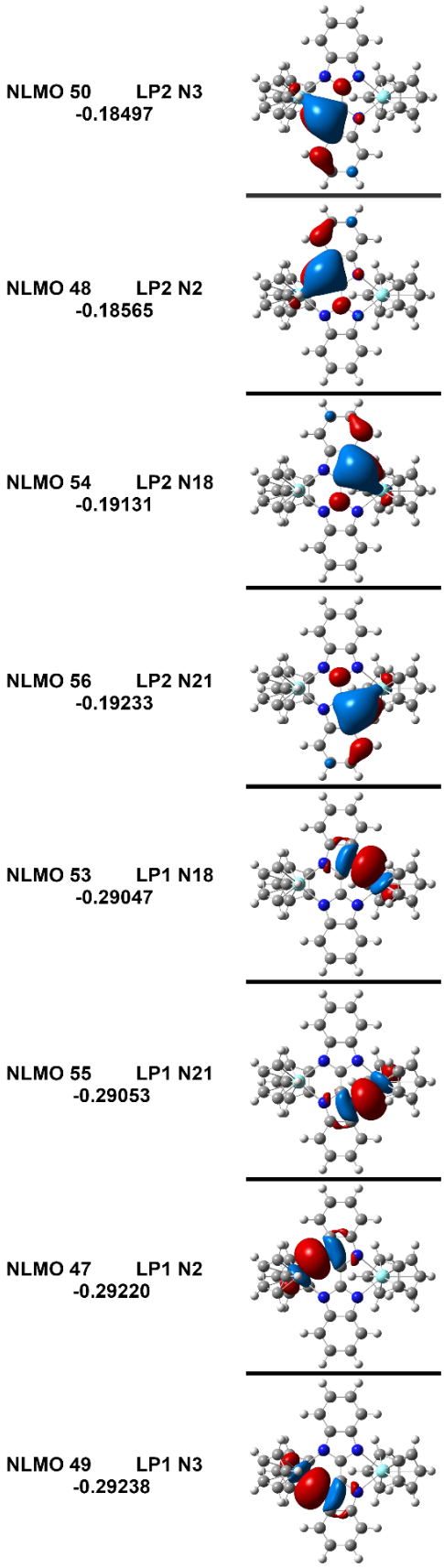

Figure S23. Graphical representation of the calculated B3LYP N lone pair NLMOs, sorted by their relative energies.

Table S13. Results of the hybridization/polarization analysis of NLMOs, given as the % contributions of parent NBOs from uB3LYP calculations on the unoptimized crystal coordinates of 1'.

		NLMO contributions α manifold					**NLMO contributions β manifold**		
NLMO No.	Description	Y1	Y24	N	NLMO No.	Description	Y1	Y24	N
47	LP1 N2	7.59	0.05	89.86	47	LP1 N2	7.75	0.06	89.68
48	LP2 N2	1.58	0.24	78.63	48	LP1 N3	7.91	0.06	89.69
49	LP1 N3	7.72	0.05	89.89	52	LP1 N18	0.06	7.61	89.78
50	LP2 N3	1.41	0.24	78.13	54	LP1 N21	0.06	7.96	89.61
53	LP1 N18	0.06	7.48	89.98					
54	LP2 N18	0.07	1.67	77.80					
55	LP1 N21	0.05	7.81	89.82					
56	LP2 N21	0.09	2.00	78.32					

Table S14. Results of the second order perturbation analysis of **2'** from uB3LYP calculations on the unoptimized crystal coordinates of **1'**. Only strongest interactions are shown (> 3 kcal/mol). Highlighted values show a significant discrepancy between α- and β-manifolds.

Donor NBO	Acceptor NBO	**E (kcal/mol) α manifold**	**E (kcal/mol) β manifold**
LP1 N2	LV1 Y1	14.94	16.15
LP2 N2	LV2 Y1	16.80	17.49
LP1 N2	LV5 Y1	19.54	19.92
LP1 N2	LV6 Y1	-	-
LP2 N2	LV4 Y1	4.09	-
LP1 N3	LV1 Y1	14.47	15.52
LP1 N3	LV2 Y1	16.45	17.60
LP1 N3	LV5 Y1	19.32	19.67
LP1 N3	LV6 Y1	-	-
LP1 N18	LV1 Y24	12.83	13.79
LP1 N18	LV2 Y24	14.52	16.30
LP1 N18	LV5 Y24	18.04	18.34
LP1 N18	LV6 Y24	-	-
LP2 N18	LV4 Y24	4.42	-
LP1 N21	LV1 Y24	14.07	14.83
LP1 N21	LV2 Y24	17.03	18.36
LP1 N21	LV5 Y24	19.42	19.72
LP1 N21	LV6 Y24	3.34	-
LP2 N21	LV4 Y24	3.92	-
LP2 N3	LV4 Y1	4.33	-

1.9 References

1 D. Small, V. Zaitsev, Y. Jung, S. V. Rosokha, M. Head-Gordon and J. K. Kochi, Intermolecular π-to-π bonding between stacked aromatic dyads. Experimental and theoretical binding energies and near-IR optical transitions for phenalenyl radical/radical versus radical/cation dimerizations, *J. Am. Chem. Soc.*, 2004, **126**, 13850–13858.

2 Q. Xiang, J. Guo, J. Xu, S. Ding, Z. Li, G. Li, H. Phan, Y. Gu, Y. Dang, Z. Xu, Z. Gong, W. Hu, Z. Zeng, J. Wu and Z. Sun, Stable Olympicenyl Radicals and Their π-Dimers, *J. Am. Chem. Soc.*, 2020, **142**, 11022–11031.

3 J. Lehner and S. Stoll, Modeling of motional EPR spectra using hindered Brownian rotational diffusion and the stochastic Liouville equation, *J. Chem. Phys.*, **152**, 094103 1-13.

4 D. E. Budil, CW-EPR Spectral Simulations: Slow-Motion Regime, in: *Methods in Enzymology*, Elsevier Inc., 1st edn., 2015, **563**, 143-170.

5 A. Sengupta and K. RM, Electron Paramagnetic Resonance Spectroscopic Investigation of the Dynamics of Spin Probe in Room Temperature Ionic Liquid, *Mod. Chem. Appl.*, 2016, **4**, 1000189 1-4.

6 H. L. C. Feltham and S. Brooker, Review of purely 4*f* and mixed-metal n*d*-4*f* single-molecule magnets containing only one lanthanide ion, *Coord. Chem. Rev.*, 2014, **276**, 1–33.

7 N. F. Chilton, R. P. Anderson, L. D. Turner, A. Soncini and K. S. Murray, PHI, *J. Comput. Chem.*, 2013, **34**, 1164–1175.